

Spontaneous periodic polarization wave in helielectric fluids

 Junchen Zhou^{a,†}, Yu Zou^{a,†}, Jinxing Li^a, Mingjun Huang^{id a,b} and Satoshi Aya^{id a,b,*}
^aAdvanced Institute for Soft Matter Science and Technology (AISMST), School of Emergent Soft Matter, South China University of Technology, Guangzhou 510640, China

^bGuangdong Provincial Key Laboratory of Functional and Intelligent Hybrid Materials and Devices, South China University of Technology, Guangzhou 510640, China

 *To whom correspondence should be addressed: Email: satoshiaya@scut.edu.cn

†J.Z. and Y.Z. contributed equally to this work.

Edited By: Cristina H. Amon

Abstract

By analogy with spin waves in ferromagnetic systems, the polarization (or dipole) wave is the electric counterpart that remains elusive. Here, we discover that the helielectricity, i.e. a polarization field with helicoidal helices that corresponds to a quasi-layered chiral nematic environment, causes a spontaneous formation of large-scale polarization waves in the form of the sinusoidal function. Both experimental and theoretical analyses reveal that the polarization ordering over a threshold polarization strength violates the inherent periodicity of the polarization helices, thus penalizing the compression energy. It drives a second-order structural transition to a periodically modulated polarization wave state. The roles of chirality and confinement condition are discussed.

Keywords: liquid crystal, ferroelectric nematic, helielectric nematic, topology, polarization wave

Significance Statement

Thanks to the mirror relationship between magnetism and electricity, similar topological natures are expected for ferromagnetic and ferroelectric systems. However, in reality, many electric analogs have yet to be found. Here, we discover that polarization waves can emerge spontaneously in chiral polar liquids. The experiments and theoretical analyses reveal that the polarization-induced violation of the quasi-layered helices drives the unprecedented spontaneous formation of polarization waves. The discovery provides a close link between ferromagnetic and ferroelectric topologies. It suggests a new pathway for generating polarization topologies in soft matter ferroelectrics.

Introduction

Ferromagnetic is a state having spontaneous magnetization, whose orientation can be changed by a magnetic field (1). Likewise, the ferroelectrics possess spontaneous polarization, which can be switched by an electric field (2). In magnetic systems, diverse topological structures characterized by modulated magnetization fields exhibit exotic quantum and ferroic properties (3–6). Especially, in recent decades, the magnetic and spin topologies have been intensively explored, like spin waves (7–9) and solitons (e.g. skyrmions (10, 11), merons (12, 13), and vortices (14–16)). On the other hand, the existence of the electric counterparts, i.e. polarization topology, and the understanding of their properties remain unclear and challenging. The strained ferroelectrics made by ceramics and alloys were the only available polar candidates for observing polarization structures in crystal forms (17–20). Very recently, the discovery of the emerging soft matter systems, including liquid crystal (LC) and some unique

polymer ferroelectrics (21–30), offers us unprecedented physical platforms with external field sensitivity and reconfigurability for investigating potential polarization topologies and the mechanisms for the manipulation and control of their dynamics.

In ferromagnetics, the competition of the Dzyaloshinskii–Moriya interactions (DMI) and Heisenberg exchange is dominant in determining the spin textures (31, 32). On the one hand, the DMI provides a helical order for the magnetic moments in ferromagnetics, whose description shares a mathematical similarity to the twist elastic energy term in LCs (31, 33). This analogy has been recently explored in the traditional chiral but apolar LCs, leading to numerous analogs of spin topology (33, 34). For example, Nych et al. (35) reported the baby skyrmion in the blue phases as an apolar version of the normal skyrmion under the confinement, which corresponds to an excitation of the topological solitary wave embedded in a uniform far-field background. On the other hand, the Heisenberg exchange interaction in ferromagnets is expressed as the magnetization gradient energy ($(\nabla M)^2$)

Competing Interest: The authors declare no competing interest.

Received: July 25, 2023. **Accepted:** July 31, 2023

© The Author(s) 2023. Published by Oxford University Press on behalf of National Academy of Sciences. This is an Open Access article distributed under the terms of the Creative Commons Attribution-NonCommercial-NoDerivs licence (<https://creativecommons.org/licenses/by-nc-nd/4.0/>), which permits non-commercial reproduction and distribution of the work, in any medium, provided the original work is not altered or transformed in any way, and that the work is properly cited. For commercial re-use, please contact journals.permissions@oup.com

(31), penalizing the distortion of the ferromagnetic order. Yet, this effect is absent in the traditional apolar LCs because the head-to-tail symmetry preserves. In the emerging ferroelectric LCs, the head-to-tail symmetry is broken, leading to spontaneous polarization. Especially in the case of the chiral and polar LCs (dubbed the helielectrics), despite the material composition and the essential interactions being distinct to ferromagnetics, the energetic scenario becomes similar. While the Hamiltonian of DMI corresponds to the twist elastic energy of the helielectrics (36, 37), the Hamiltonian of the Heisenberg exchange interaction resembles the polarization gradient energy in LCs ($(\nabla P)^2$) that has not been explored so far. By this analogy, we anticipate various unprecedented polarization topologies exhibiting similar polar fields to those in ferromagnetics. Here, we report on a large-scale assembly of the sinusoidal polarization solitary wave in the emerging helielectric nematic (HN*) state. In contrast to the external field-assisted instant generation of orientational waves in apolar systems (e.g. the so-called Helfrich–Hurault instability in traditional chiral and layered LCs and 2D inorganics colloids (38–42)), the discovered polarization wave is not due to the structural instability but forms spontaneously as a new ground state, which results in periodic polarization arrays. Using confocal second-harmonic generation microscopy (C-SHGM) imaging, we visualize the polarization field. A minimal mean-field analysis reveals that the spontaneous formation of the periodic polarization waves (PPWs) corresponds to a second-order transition from a uniform helical state upon increasing the polarization strength of the system.

Results

To obtain the HN* state, we employed several ferroelectric nematic (N_F) LCs, RM734 (21) and A2, as the host material and added different chiral dopants, e.g. R811 and S1 (36) (Materials and methods and Scheme S1). The HN* materials are then introduced into homemade LC cells under the syn-parallel rubbing condition. This leads to the same polarization direction on the top and bottom surfaces in the polar phases. The tested LC mixtures have a fixed phase sequence during the cooling process, i.e. from the isotropic liquid (Iso) to the traditional apolar chiral nematic (N^*) and then to the HN* state. The ensemble-averaged molecular orientation, the so-called director \mathbf{n} , in the apolar nematic and N^* phases is head-to-tail equivalent (Fig. 1A and B). The inversion symmetry is broken in the N_F and HN* states where the polarization order emerges (Fig. 1C and D). In the N^* state (Fig. 1B), the helical pitch ($P_{N^*} = 2\pi K_{22}/K'_{22}$) is purely determined by the elastic competition between the twist elasticity term ($K_{22}[\mathbf{n} \cdot \nabla \times \mathbf{n}]^2$) and the magnitude of the chirality ($K'_{22}[\mathbf{n} \cdot \nabla \times \mathbf{n}]$) (38). On the other hand, in the HN* state (Fig. 1D), the local ferroelectric order tends to prevent the polarization field from distortions, mainly attributed to the effect of the gradient term in the free energy function (36, 43). This consequence permits the helielectric pitch (P_{HN^*}) to produce the self-dilation so that the pitch length is longer in the HN* state than that in the N^* state, even under the same elastic conditions. Since the helical pitch of the HN* state cannot be fully extended in the LC cell due to the space constraint imposed by the strong surface polarization anchoring, then a question arises: what kind of polar structure will develop at the equilibrium?

Figure 2A–F summarizes three representative examples of micrograph textures of HN* materials under polarizing light microscopy (PLM). In the N^* state, due to the strong planar surface anchoring, the helical axis of the director is uniformly along the surface normal. This results in uniform Grandjean textures

(Fig. 2A and B). With decreasing temperature to the HN* state, the nucleation and the subsequent full coverage of a 2D grid-like pattern spontaneously occurs (Fig. 2C–F). The grid size increases with increasing the pitch length of the sample, which is also supported by our theoretical calculations (Fig. S1). Importantly, though similar apolar analogs can be observed in apolar LC systems through field-driven Helfrich–Hurault mechanisms (39, 44), they arise as a result of transient instability and have considerable differences from the current situation as discussed below. Next, to analyze the 3D polarization structures of the grid-like pattern, we combined fluorescence confocal polarization microscopy (FCPM) that probes the orientational field (Fig. S2) and C-SHGM (Fig. S3), which visualizes the spatial distribution of polarization. By fully reconstructing the 3D polarization structures, we clarify that the development of the grid-like pattern is a dynamic process, where each grid corresponds to a topological soliton protected by a pair of disclinations as discussed below, and these localized waves assemble a global 2D-confined undulated polarization wave composed of polar helices. Hereafter, we name it the PPW (Fig. 2G–N). The doubled periodicity of the bright-dark layers in the 2D and 3D C-SHGM images corresponds to a quasi-layer composed of a full pitch of the polarization helices. Figure 2I–N shows the transitional process from the uniform state to the PPW state. While, at the early stage of the formation of PPW, the polarization structure is in a sinusoidal form (Fig. 2J), it gradually develops into more asymmetric structures as the temperature decreases (Fig. 2K; Fig. S4). As seen in the xz plane, the quasi-layers of PPW bend with larger amplitudes away from the surfaces (Fig. 2J and K). Particularly, at the late stage of the PPW formation, PPW deviates from a pure sinusoidal form, which exhibits a pair of disclinations with nonsingular cores, $\lambda_{+1/2}$ and $\lambda_{-1/2}$ (Fig. S5) (39), arranging periodically on the top and bottom surfaces (Fig. S6). Besides, the tilting of the quasi-layers relies on the chirality of systems: left- and right-handed dislocation forms in left- and right-handed systems by doping with different types of chiral dopants (Figs. S5 and S7). Combined with the xy cross-sectional image of C-SHGM near the middle of the LC cell (Fig. 2I–N), one can directly see that the grid-like pattern is regularly packed at the equilibrium and accompanies a periodic undulation of the polar helices.

Distinct from the field-driven undulation instability in apolar LC systems where the undulation disappears unless an external field is applied (39, 44), PPW forms spontaneously under several conditions as discussed below. Figure 3 demonstrates the representative PLM evolution for 5 wt% S1/RM734 mixture and spatial coverage of the grid-like patterns as a function of temperature for the long- and short-pitch helielectrics. The first incidence of the grid-like pattern comes upon the N^* –HN* transition (Fig. 3B), which persists only for <1 K right upon the phase transition and goes into the Grandjean texture (Fig. 3C). The transient pattern appears as a result of the inhomogeneous quasi-layer (so the helices) formation and are not macroscopically polar (so is Not the PPW). Once the relevant phase transition completes and the phase reaches equilibrium, the pattern becomes unstable (Fig. 3D). Decreasing temperature to low temperatures of the HN* state results in the second time of incidence of the grid-like pattern, i.e. PPW (Fig. 3E). For this time, the polarization structure remains stable down to low temperatures until crystallization happens (Fig. 3F) and the generation rate decreases as the cooling rate decreases (Fig. S8). By varying the concentration of the chiral agent S1, we clarify that the same structural transitional behavior is observed under different helielectric pitches (Fig. 3G). It is worth noting that while the observed PPW is an orientational analog to the recently discovered atomic dipole wave found in $\text{PbTiO}_3/\text{SrTiO}_3$

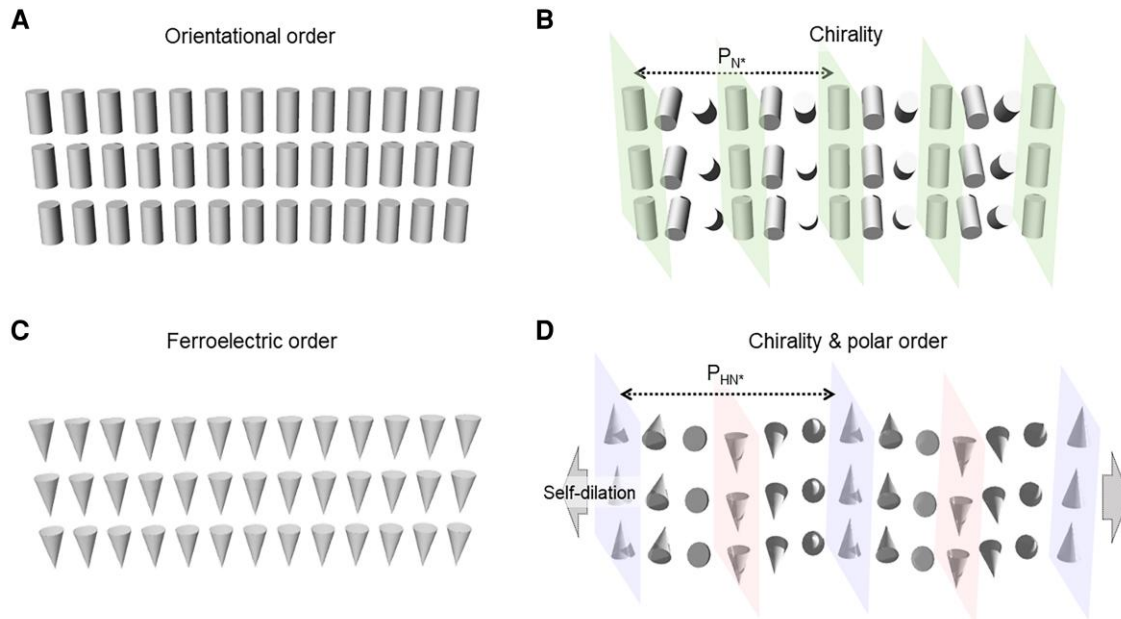


Fig. 1. Schematics of orientational fields for N A), N* B), N_F C), and HN* D) states. A) The cylinders represent the head-to-tail equivalent \mathbf{n} director in the apolar nematic. B) The N* state with a quasi-layered helical structure is formed after the introduction of chirality into the apolar nematic. The quasi-layer distance corresponds to a half pitch of the helix. C) The cones represent the polarizations in the N_F state. D) The HN* state is formed after the introduction of chirality in the polar nematic, where the helielectric pitch P_{HN^*} is elongated due to the competition between the chiral and polar orders. In contrast to the N* state, the quasi-layer distance herein corresponds to a full pitch of the helix.

superlattice (45) and has a similar orientation structure with spin waves in ferromagnetics (46), although they are distinct in the formation's origins. As discussed in detail later by a minimal model, in contrast to spin waves driven by the exchange interactions between local spins (47), the formation of PPW results from the competition between the elasticity and polarity of the ferroelectric LCs. Recall that the ferroelectric ordering in the helielectrics linearly couples to an electric field. Applying a direct-current field horizontally to the system forces the PPW to be screened along the electric field, which leads to a manipulation of the 2D PPW to the 1D PPW with their stripes parallel to the electric field (Fig. S9). After removing the electric field, 2D PPW recovers (Fig. S10), confirming that PPW is the lowest energy state. The switchability enables the transformation of PPW to serve as a reconfigurable optical grating (Fig. S11).

In addition to the temperature conditions, the sample thickness also plays a vital role in stabilizing the formation of PPW. Figure 4A and B demonstrates PLM textures for the N* and HN* states in a syn-rubbed wedge cell, where the sample thickness continuously increases from the left to right side. One finds that the Cano line divides the field of view into several areas, hereafter named the Cano band (Fig. 4A and B). While the two neighboring Cano bands in the apolar N* state differ by a half-pitch variation of the helices (Fig. 4A) (48, 49), the pitch variation becomes a full pitch in the polar HN* state (Fig. 4B). Therefore, the width of Cano bands in the HN* state roughly doubles compared with that in the N* phase (28, 36). Observing the extremely thin areas of the wedge cell, one notices that no PPW is formed even if the aforementioned temperature requirement is met (see Figs. 3 and 4B). In this situation, while the bulk favors the PPW formation, the spatial confinement along the sample thickness direction suppresses the incidence. Only when the sample thickness is large enough PPW emerges in the thicker areas of each Cano band (Fig. 4B; areas indicated by purple bars), where both the occupation ratio of PPW in each Cano band and the wavelength of PPW

increase with increasing the sample thickness (Fig. 4C; Fig. S12). It is worth noting that the threshold thickness for inducing PPW decreases as the helielectric pitch decreases, which is supported by our theoretical analyses (Section S3). It is known that the actual pitch length of the chiral LCs changes continuously with the thickness in each Cano band due to the variation of the sample thickness and fixed anchoring conditions on surfaces (28, 36). The same scenario applies to the HN* state. As evidenced by our theoretical analyses later, this consequence gives rise to a comparable competition between the spatial confinement (*suppressing* PPW) and polar interactions (*favoring* PPW), thus leading to the coexistence of PPW and undeformed helices, especially in the middle range of the sample thicknesses. Furthermore, when PPW arises, the Cano lines change their morphology from a straight line to a wavy curve (Fig. 4D; Fig. S13). This phenomenon would be attributed to the periodic directional variation of polarizations in PPW, which causes the corresponding periodic modulation of the Cano lines. So far, we reveal two essential characteristics for the induction of PPW: (i) PPW appears only at the low temperatures of the polar HN* state; and (ii) PPW is suppressed when the confinement condition is inappropriate.

Discussion

To understand the physical mechanism of the PPW formation in the HN* state, we established a minimal model that corresponds to an extended Frank–Oseen formalism under the single-elastic constant approximation. Let us assume that the polarization $\mathbf{P} = (P_x, P_y, P_z)$ is parallel to the local director, i.e. $\mathbf{P} = P_0 \mathbf{n}$, and that the helielectrics start to deviate from a uniform z-orientated polarization helix, $\mathbf{n}_0 = \cos(qz)\mathbf{x} + \sin(qz)\mathbf{y}$, to the PPW state. q is the wavenumber of the polarization helix (the inverse of the helical pitch $P_{HN^*} = 2\pi/q$). To consider the quasi-layer nature of the polarization helices, we introduce the layer displacement as $u = A \sin(tz) \cos(kx) \cos(ky)$ satisfying the experimentally observed

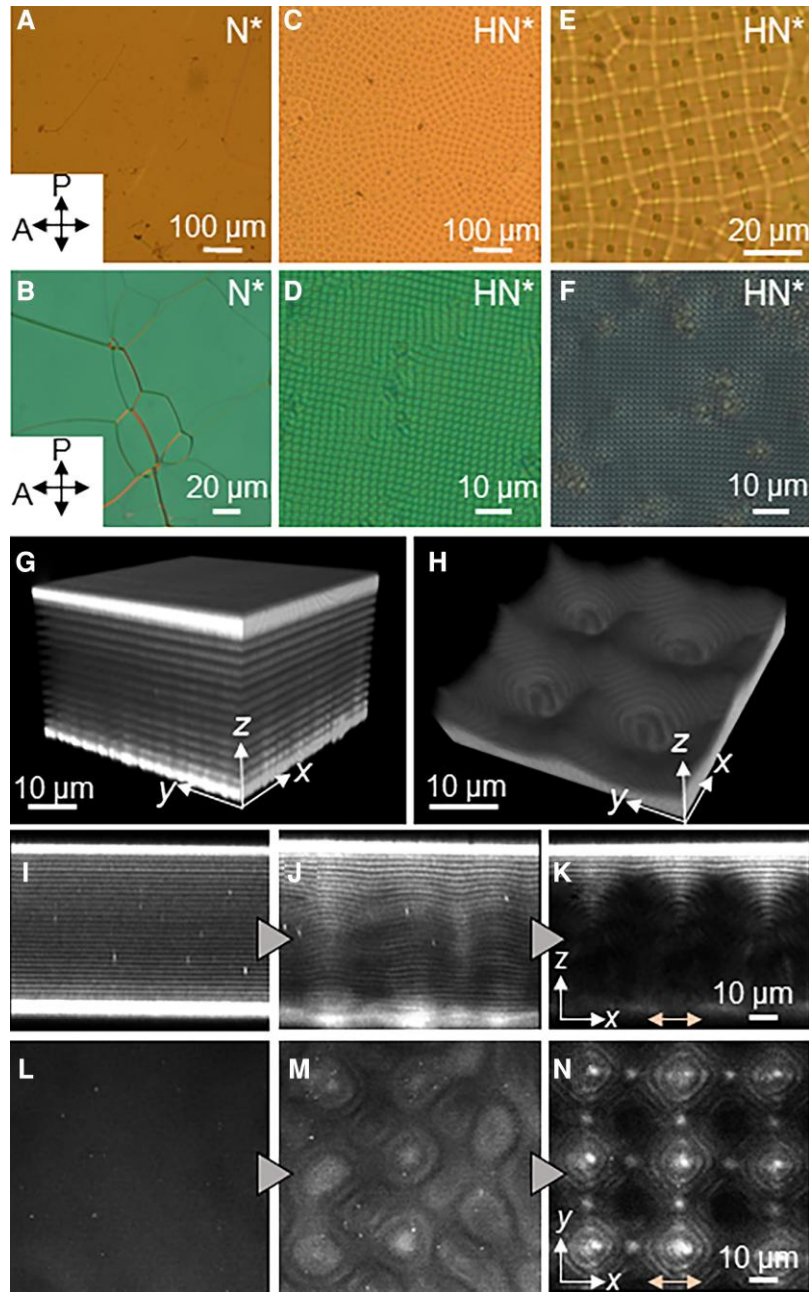


Fig. 2. PLM and C-SHGM images of PPW in the HN* state. A–F) PLM texture evolution of 5, 30, and 50 wt% S1/RM734 mixtures during cooling. Uniform Grandjean texture of 5 wt% S1/RM734 at 135°C A) and 30 wt% S1/RM734 at 120°C B). PPW in 5 wt% S1/RM734 at 75°C C), in 30 wt% S1/RM734 at 40°C D), and in 50 wt% S1/RM734 at 30°C F). E) Expanded view of PPW in 5 wt% S1/RM734 at 75°C. The periodicity of PPW in E), D), and F) is 15.5, 2.0, and 1.5 μm , respectively. The cell thicknesses are 50 μm for 5 wt% S1/RM734 and 5 μm for 30 and 50 wt% S1/RM734 mixtures. All the cells are rubbed syn-parallelly in the horizontal direction. G, H) The 3D reconstructed polarization structures from the pseudo layer to PPW. I–N) C-SHGM images of PPW in 1 wt% R811/A2 mixture. The xz I, K) and xy (L–M) cross-sections of PPW are visualized by a linear polarization (the yellow double arrow). The temperatures are 80°C, 70°C, and 50°C from left to right, respectively. The helical pitches for 5 wt% S1/RM734, 30 wt% S1/RM734, 50 wt% S1/RM734, and 1 wt% R811/A2 mixtures are 5.6, 0.8, 0.4, and 4.8 μm , respectively. The cell thicknesses are 50 μm for 5 wt% S1/RM734 and 5 μm for 30 and 50 wt% S1/RM734 mixtures.

conditions upon the onset of PPW (50), which leads to the deformed polarization field as follows:

$$\mathbf{n} = [\cos(qz) + uq\sin(qz)]\mathbf{x} + [\sin(qz) - uq\cos(qz)]\mathbf{y} + \left[\frac{\partial u}{\partial x} \cos(qz) + \frac{\partial u}{\partial y} \sin(qz) \right] \mathbf{z} \quad (1)$$

A, t, and k are the amplitude of displacement, the wavenumber of the displacement along the z direction, and the wavenumber of

the displacement in the xy plane, respectively (Fig. 5A). Then, the extended Frank–Oseen free energy functional with minimal terms is described as follows:

$$f_{\text{bulk}} = \frac{K}{2} \left(\frac{\partial^2 u}{\partial x^2} + \frac{\partial^2 u}{\partial y^2} \right)^2 + \frac{B}{2} \left[\frac{\partial u}{\partial z} - \frac{1}{2} \left(\frac{\partial u}{\partial x} \right)^2 - \frac{1}{2} \left(\frac{\partial u}{\partial y} \right)^2 \right]^2 + \frac{\tau_1}{2} \mathbf{P}^2 + \frac{\tau_2}{2} \mathbf{P}^4 + \frac{h}{2} (\nabla \mathbf{P})^2, \quad (2)$$

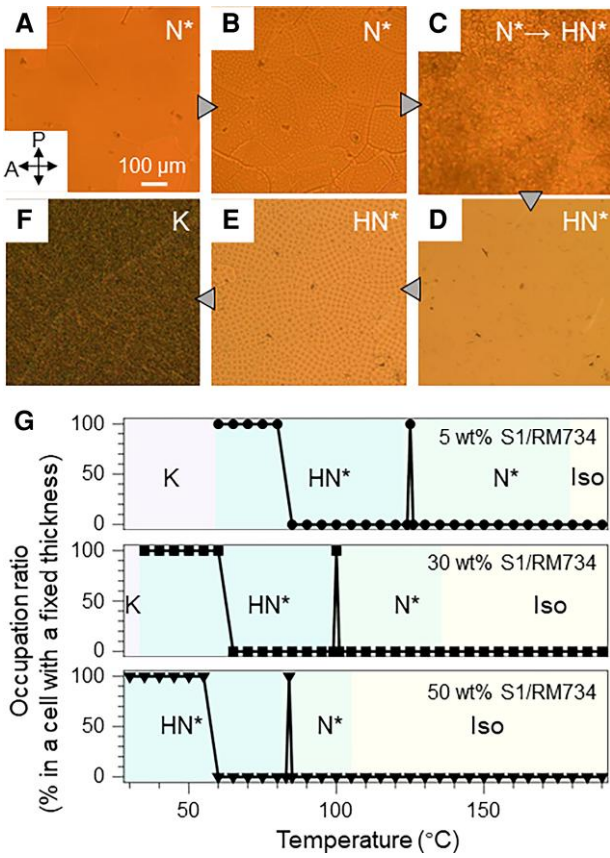


Fig. 3. Evolution from the uniform helical state to PPW upon cooling process. A–F) PLM images upon cooling in 5 wt% S1/RM734 mixture from the N* to HN* state. The temperatures are 150°C (A), 125°C (B), 124°C (C), 110°C (D), 75°C (E), and 30°C (F), respectively. G) The temperature dependence of the occupation ratio of PPW for 5, 30, and 50 wt% S1/RM734. The cell thicknesses are 50 μm for 5 wt% S1/RM734 and 5 μm for 30 and 50 wt% S1/RM734 mixtures. The cooling rate for the observations is fixed to be 5 K/min.

$$f_{\text{surf}} = \frac{1}{2} W_0 \left[\left(\frac{\partial u}{\partial x} \right)^2 + \left(\frac{\partial u}{\partial y} \right)^2 \right]. \quad (3)$$

The first two bulk terms describe the elastic and compression free energies, where K and B are the elastic coefficients with a relationship of $B = Kq_0^2$ under the single-elastic constant approximation (39). We assume that compression energy arises simply due to the layer displacement, not affected by the polarity of the system. The third and fourth bulk terms are the Landau energy, which accounts for the stability of a polar phase. $\tau_1 = \alpha(T - T_0)$ is the scaled temperature with respect to the critical temperature T_0 for the apolar-polar LC transition, i.e. the N*–HN* transition. τ_2 is a phenomenological coefficient for the higher-order terms (\mathbf{P}^4) in Landau energy. The Landau coefficients can describe the equilibrium polarization strength of the system as $-\tau_1/2\tau_2 = P_0^2$. The last bulk term is the polarization gradient energy with a coefficient $h > 0$. It penalizes the spatial variation of the polarization field due to $(\nabla \mathbf{P})^2 = \sum_{ij} (\partial_i P_j)^2$ ($i, j \in x, y, z$) and has the same form as

the Heisenberg exchange interactions (or magnetization gradient energy) in ferromagnetic materials (31, 51), i.e. $J(\nabla \mathbf{M})^2$. In addition, the LC cell surfaces ($z = 0, d$) are considered to impose a uniform planar alignment along the x direction, corresponding to the

rubbing-induced polarization anchoring in the experiments. The surface anchoring strength is controlled by W_0 . f_{surf} is the surface free energy. W_0 is the magnitude of the planar surface anchoring (i.e. anchoring of layers parallel to the substrates). It is worth noting, according to our calculation, that the flexoelectricity and space charge effects are not essential for inducing PPW, which just slightly modify the structural feature of PPW (Fig. S14 and Section S4). Therefore, for simplicity of the following analysis, we do not include these effects. By the course-grained method (38, 39, 50), the average free energy over a full PPW periodicity is calculated as follows:

$$\bar{f} = \frac{\int_0^d \int_0^{2\pi} \int_0^{2\pi} f_{\text{bulk}} dx dy dz}{\int_0^d \int_0^{2\pi} \int_0^{2\pi} dx dy dz} + \frac{\int_0^{2\pi} \int_0^{2\pi} f_{\text{surf}} dx dy}{\int_0^{2\pi} \int_0^{2\pi} dx dy} = \frac{1}{4} W_0 A^2 k^2 \sin^2 dt + C_1 t^2 + C_2 t \sin(2td) + C_3 \frac{\sin(2td)}{t} + C_4, \quad (4)$$

$$C_1 = \frac{1}{16} A^2 [B + hP_0^2(k^2 + q^2)], \quad (5)$$

$$C_2 = \frac{C_1}{2d}, \quad (6)$$

$$C_3 = \frac{A^2 [5A^2 B k^4 \cos(2dt) - 20A^2 B k^4 - \rho]}{2,048d}, \quad (7)$$

$$C_4 = \frac{15A^4 B k^4 + 512P_0^2(hq^2 + \tau_1 + \tau_2 P_0^2) + \rho A^2}{1,024}, \quad (8)$$

$$\rho = 64[2k^4(2K + hP_0^2) + hP_0^2 q^4 + 3hk^2 P_0^2 q^2]. \quad (9)$$

Under the strong planar anchoring on the surfaces, we set the sample thickness d to be the integer times of the helical pitch of HN* ($d = N \cdot 2\pi/q$) if the top and bottom surface polarizations align in the same direction (i.e. syn-parallel rubbing condition). N is the number of the full pitch of HN*. Therefore, the lowest mode of the modulation of the layer displacement along the z direction, t , is related to the thickness of the cell, i.e. $t = \pi/d$ (Fig. 5A). We minimize the free energy with respect to k^2 and obtain the equilibrium wavenumber of the modulation in the xy plane, $k_0 = 2\pi/\Lambda$ (Eq. 10). By inserting k_0 into Eq. (4), the minimal average free energy can be obtained.

$$\frac{\partial \bar{f}}{\partial k^2} \Big|_{k=k_0} = 0 \Rightarrow k_0^4 = \frac{1,024P_0^4(h\pi^2 + 3hd^2q^2)}{d^4(15A^2B + 256K + 128hP_0^2)}, \quad (10)$$

$$\bar{f} = \frac{\beta A^4 + \delta A^2 - \kappa A^2 + 64P_0^2(2K + hP_0^2)(hq^2 + \tau_1 + \tau_2 P_0^2)}{15A^2B + 128(2K + hP_0^2)}, \quad (11)$$

$$\beta = \frac{15B[B\pi^2 + hP_0^2q^2(\pi^2 + d^2q^2)]}{16d^2}, \quad (12)$$

$$\delta = \frac{32KB\pi^2 + BP_0^2[h(16\pi^2 + 15d^2q^2) + 15d^2(\tau_1 + \tau_2 P_0^2)]}{2d^2}, \quad (13)$$

$$\kappa = \frac{hP_0^2[hP_0^2(\pi^2 - d^2q^2)^2 - 16d^2Kq^2(\pi^2 + d^2q^2)]}{d^4}. \quad (14)$$

Let us first discuss when one finds PPW spontaneously forms in a z -orientated HN* helix with a fixed thickness, d being a constant. This corresponds to the temperature requirement for achieving PPW as observed in Fig. 3. Recalling the spontaneous formation of PPW is only achieved at low temperatures of the HN* state (Fig. 3G), we investigate how the polarity and elasticity affect the stability of PPW. If PPW arises spontaneously, then the deformation amplitude A becomes a nonzero real number at the free energy minimum (Eq. 11). Minimizing the

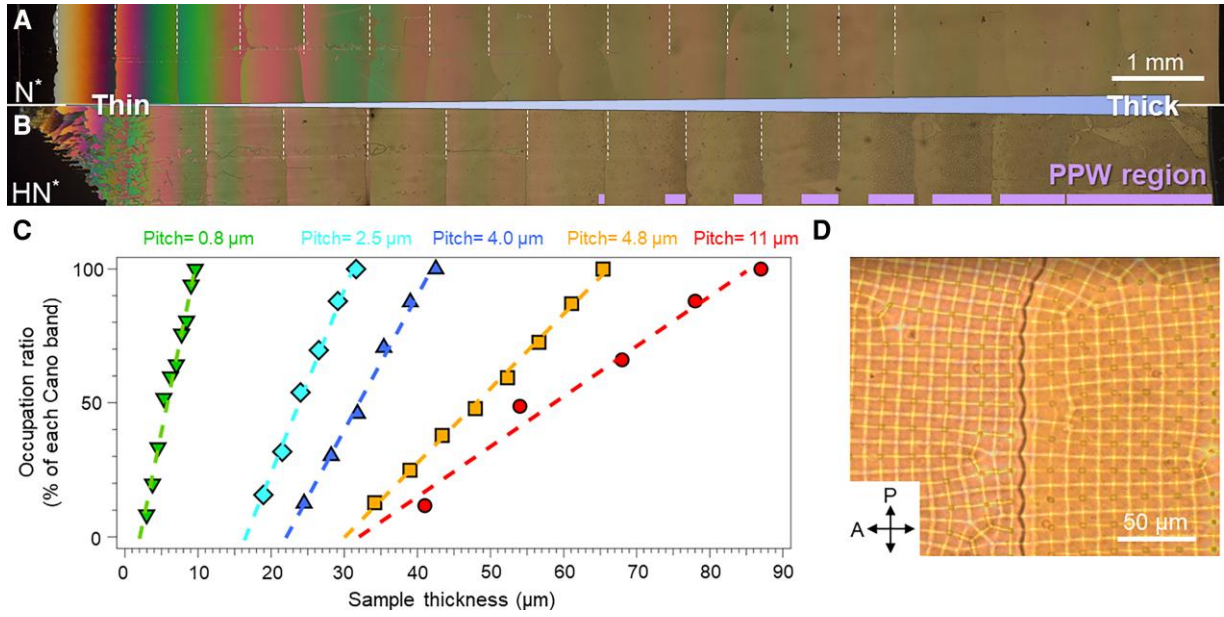


Fig. 4. PLM images of the 1 wt% R811/A2 mixture in a wedge cell. A) The N^* state at 130°C. B) The HN^* state at 30°C. The wedge angle of the cell is $\tan\theta = 0.006$. C) The relationships between the occupation ratio of the PPW in each Cano band and the sample thickness under different LC mixtures conditions are plotted. The dashed lines are the linear fittings. The corresponding doping ratios of R811 in A2 for the samples are 0.5 (red circles), 1.0 (orange squares), 1.5 (blue upward triangles), 2.0 (cyan rhombi), and 30 wt% (green downward triangles), respectively. D) A PLM image of a wavy Cano band separating two Cano bands with PPW fully developed (1 wt% R811/A2 mixture).

free energy (Eq. 11) with respect to A leads to the solution of the equilibrium amplitude A_0 :

$$\frac{\partial \bar{f}}{\partial A} = 0 \Rightarrow A_0^2 = \frac{32(2K + hP_0^2)}{15B} \left\{ \frac{\sqrt{2}hP_0^2(\pi^2 + 3d^2q^2)}{d\sqrt{(2K + hP_0^2)[B\pi^2 + hP_0^2q^2(\pi^2 + q^2d^2)]}} - 4 \right\}. \quad (15)$$

It is clear that the magnitude of the polarization of the system, P_0 , plays a critical role in stabilizing PPW. $A_0^2 < 0$ when P_0 is zero or small; therefore, no real value of A_0 exists, which corresponds to the apolar N^* state. Under this circumstance, PPW is absent, consistent with the experimental observation that no spontaneous modulated N^* structures have been observed so far. With increasing the polarization P_0 over a certain threshold P_H , PPW becomes energetically favorable with a finite amplitude of the modulation ($A_0 \neq 0$). By solving P_H based on the condition $A_0^2 > 0$, we find the analytical solution:

$$P_H^2 = \frac{4d \left\{ \zeta + \sqrt{\zeta^2 + \pi^2 BK(\pi^2 - d^2q^2)^2} \right\}}{h(\pi^2 - d^2q^2)^2}, \quad (16)$$

$$\zeta = d[B\pi^2 + 2Kq^2(\pi^2 + d^2q^2)]. \quad (17)$$

Over P_H , the amplitude A_0 in the PPW increases with the increase of polarization (Fig. 5B; Eq. 15). To visualize how the polarization strength modifies the free energy landscape, we show the free energy curves as a function of the modulation amplitude A (Fig. 5A), obtained by numerically calculating Eq. (11). At low P_0 values ($P_0 \leq P_H$), there is a single minimum at $A_0 = 0$, corresponding to an undeformed HN^* helix. At $P_0 > P_H$, two non-zero minima appear at $A_0 \neq 0$. Note that there is no energy barrier between the states with $A_0 = 0$ and $A_0 \neq 0$ upon the spontaneous transition to the PPW state, suggesting the structural transition is second-order like. Indeed, in the experiments under a fixed sample thickness, we observe the PPW formation accompanied by a pretransitional orientational fluctuation. The

modulated structure of PPW gradually appears without a coexistence with the uniform regions. To compare the real situation with the theoretical prediction, we measure the spontaneous polarization of the polar LCs as a function of temperature (Fig. 5B; Fig. S15). The spontaneous polarization increases with decreasing temperature after going into the HN^* state due to the higher polar order. In our numerical calculation, we fixed the parameters [K , q , d , τ_1 , τ_2 , and h] to be [10^{-6} dyn, $1.12 \mu\text{m}^{-1}$, $30 \mu\text{m}$, $-6 \times 10^{-7} \text{J}\cdot\text{m}^3/\text{C}^2$, $1.875 \times 10^{-4} \text{J}\cdot\text{m}^7/\text{C}^4$, and $10^{-5} \text{J}\cdot\text{m}^3/\text{C}^2$], whose condition of the helical pitch corresponds to the ground state pitch of the 5 wt% S1/RM734 mixture. We change the polarization strength P_0 at each temperature according to the experimental values for the numerical analyses. The calculated equilibrium amplitudes of PPW at each temperature are plotted in Fig. 5B. The experimental and predicted temperature ranges of PPW by the theory are well consistent. Meanwhile, we also find that the increase of the nematic elasticity with decreasing temperature would destabilize PPW (Fig. S16 and Section S2). Therefore, we conclude that the spontaneous formation of PPW in the HN^* state should be attributed mainly to the large-enough polarization in the polar LCs at low temperatures.

Now, let us move to the second discussion on the stability of PPW in confinement (Figs. 4A–C and 6A). Figure 6A depicts the geometry and HN^* helical arrangement in a Cano band that contains N numbers of full helielectric pitches in the wedge cell. Due to the sample thickness gradient, the helielectric pitch ($2\pi/q$) varies with thickness in the range of $2\pi(N-1)/q_0$ to $2\pi N/q_0$, where q_0 is the equilibrium helielectric pitch in the bulk. To implement this scenario in our analysis, we now treat the sample thickness d as a variable, so that q becomes a variable as $d = N \cdot 2\pi/q$. By this scheme, we can address whether PPW arises under confinement conditions with variable sample thicknesses in a particular Cano band. To simplify the calculation, we ignore the quartic term of Landau energy (43) in Eq. (11), which has a minor effect in

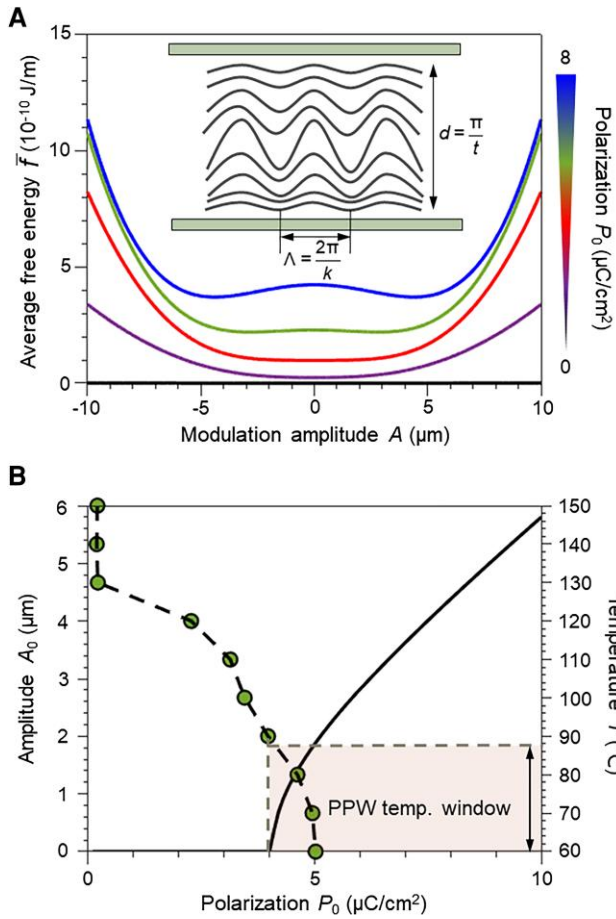


Fig. 5. The role of polarization on the stability of PPW. A) The average free energy as a function of the modulation amplitude for the systems with different polarization is plotted in different colors. Their polarization strengths for the numerical calculations are set to be 0 (black), 2 (purple), 4 (red), 6 (green), and 8 $\mu\text{C}/\text{cm}^2$ (blue). Here, we set the elastic constant $K = 10^{-6}$ dyn, cell thickness $d = 30$ μm and helielectric pitch $P_{\text{HN}^*} = 5.6$ μm , respectively. τ_1 , τ_2 , and h are set to be -6×10^{-7} $\text{J}\cdot\text{m}^3/\text{C}^2$, 1.875×10^{-4} $\text{J}\cdot\text{m}^7/\text{C}^4$, and 10^{-5} $\text{J}\cdot\text{m}^3/\text{C}^2$, respectively. The inset shows a 2D model of the inset structure of PPW formed in the LC cell under a fixed thickness. Λ represents the wavelength of PPW. B) The scattered points connected by a dashed line are the experimentally measured polarization as a function of temperature. The black solid line is the numerical calculation results on the equilibrium amplitude of PPW as a function of the polarization strength of the system, where the experimentally measured polarization data as a function of temperature is used. The other parameters used for the numerical calculation are the same as those in A). According to the numerical solutions, the threshold polarization for generating PPW is about 4.06 $\mu\text{C}/\text{cm}^2$. This predicts the temperature range of the PPW state is about 89 $^\circ\text{C}$, in line with the experimental observation (Fig. 3B, top).

affecting the stability of PPW, and obtain the equilibrium amplitude A_0 of PPW as

$$A_0^2 = \frac{16\sqrt{2K + hP_0^2}}{15B} \left\{ \frac{\sqrt{2P_0^2q} \left| h + 12hN^2 + \frac{4\tau_1 N^2}{q^2} \right|}{N\sqrt{B + P_0^2q^2} \left(h + 4hN^2 + \frac{4\tau_1 N^2}{q^2} \right)} - 8\sqrt{2K + hP_0^2} \right\}. \quad (18)$$

When q is large, corresponding to a small helielectric pitch for the HN^* state, PPW is absent because of $A_0^2 < 0$. When q is below to

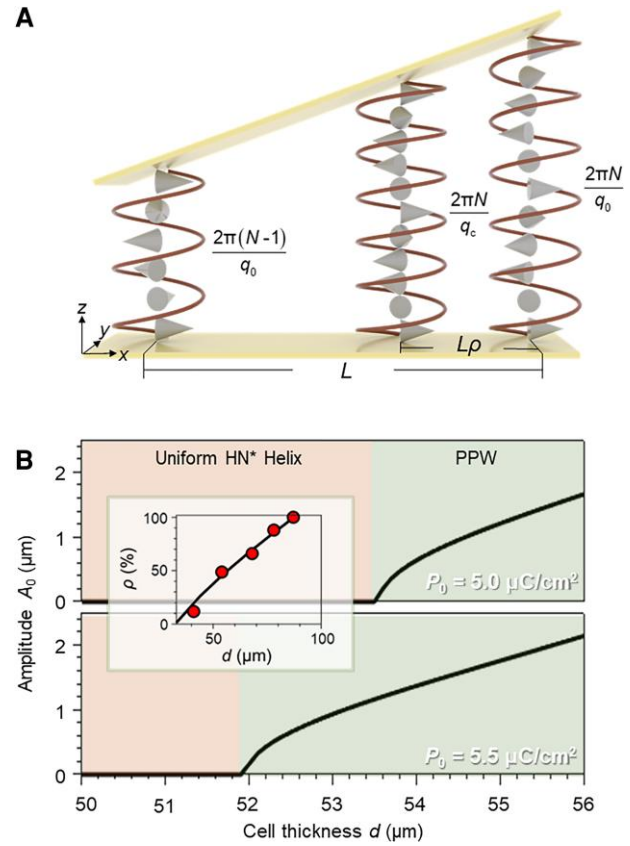


Fig. 6. The role of the confinement condition on the stability of PPW. A) Schematics of a Cano band formed by HN^* LCs in a wedge cell. B) The numerical calculation results on the amplitude of PPW as a function of the thickness in the Cano band under different polarization strengths (5.0 $\mu\text{C}/\text{cm}^2$ for the top and 5.5 $\mu\text{C}/\text{cm}^2$ for the bottom figures). We set the equilibrium pitch length to be 5.6 μm and the thickness of the Cano band in the range of 50 to 56 μm with $N = 10$. τ_1 and h are set to be -6×10^{-7} $\text{J}\cdot\text{m}^3/\text{C}^2$ and 6×10^{-7} $\text{J}\cdot\text{m}^3/\text{C}^2$, respectively. The inset shows the relationship between the thickness and the occupation ratio of PPW in each Cano band. The red scattered points are the experimentally measured occupation ratio as a function of the sample thickness for 0.5 wt% R811/A2 mixture. The helical pitch for this sample is 11 μm . The numerical calculation result fitted by Eq. (22) is plotted by the solid line. In our fitting, we set the equilibrium pitch length to be 11 μm , the elasticity coefficient $K = 10^{-6}$ dyn and the polarization strength $P_0 = 4.5$ $\mu\text{C}/\text{cm}^2$. τ_1 and h are set to be -2.5×10^{-7} $\text{J}\cdot\text{m}^3/\text{C}^2$ and 6×10^{-6} $\text{J}\cdot\text{m}^3/\text{C}^2$, respectively.

a critical value q_c as

$$q_c^2 = \frac{4N^2\eta \left[4B\eta + \varpi - 2\sqrt{2\eta(2B^2\eta + 64\tau_1^2KP_0^2N^4 + B\varpi)} \right]}{hP_0^2 \left[h^2P_0^4(1 - 4N^2)^2 - 2KhP_0^2(112N^4 + 40N^2 - 1) - 128K^2(4N^4 + N^2) \right]}, \quad (19)$$

$$\eta = 2K + hP_0^2, \quad (20)$$

$$\varpi = \tau_1P_0^2[32N^2K + h(4N^4 - 1)P_0^2], \quad (21)$$

$A_0^2 > 0$, i.e. PPW ($A_0 \neq 0$), becomes favorable and develops spontaneously from the undeformed HN^* helix ($A_0 = 0$). These results mean that if the helielectric pitch is strongly compressed, PPW is unstable and forms only in the region of a Cano band where the sample thickness is larger than the critical thickness $d_c = 2\pi N/q_c$. Notably, q_c decreases for distinct Cano bands with smaller values of N (Fig. S17). Too small values of N , corresponding to extreme-thin sample thicknesses results in $q_c \leq q_0$, thereby

PPW does not appear in the corresponding Cano bands because d_c is equal to or is larger than the maximum thickness $2\pi N/q_0$ of the Cano band (Fig. 6A). In the Cano bands with intermediate sample thicknesses, the condition $q_0 \leq q_c \leq Nq_0/(N-1)$ is satisfied, leading to the appearance of PPW in thicker areas of a Cano band. Once the sample thickness is too thick, so $q_c \leq q_0$, Cano bands are then fully covered by PPW. As direct visualizations of how PPW covers Cano bands at the intermediate sample thickness conditions, we plot numerical calculation results on the spatial distribution of the amplitude of PPW in a Cano band with moderate sample thicknesses ($50 < d < 56 \mu\text{m}$, $q_0 = 5.6 \mu\text{m}$; Fig. 6B). As seen from the analytical solutions, the numerical results also confirm that PPW develops only in the thicker region of the Cano band. The amplitude of PPW increases with the sample thickness. Increasing the polarization strength of the system results in the larger spatial occupation of PPW, ρ . Furthermore, according to the geometry conditions of the confinement as depicted in Fig. 6A, we obtain the quantitative relationship between d and ρ (Fig. 4C) as

$$\tan \theta = \frac{2\pi N \left(\frac{1}{q_0} - \frac{1}{q_c} \right)}{L\rho} \Rightarrow \rho = \frac{1}{L \tan \theta} \left(\frac{2\pi N}{q_0} - \frac{2\pi N}{q_c} \right). \quad (22)$$

θ is the angle of the wedge cell. L represents the width of each Cano band. The inset of Fig. 6B demonstrates the good prediction of ρ as a function of d in a long-pitch helielectric (0.5 wt% R811/A2 mixture), in line with the experimental results.

To conclude, we experimentally observed the spontaneous formation of PPW in polar and chiral LC systems. We showed both the analytical and numerical solutions based on an extended Frank–Oseen free energy functional for explaining the generation conditions of PPW. In line with the fact that the exchange and DM interactions in ferromagnetic materials are crucial to spin topology, our study confirms that, in electric systems, the coupling between the polarization of a system and nematic elasticity is an important driving force for generating unprecedented polarization topology. The results suggest a close link between ferroelectric and ferromagnetic topologies. Our work will help understand the formation of topology in the ferroelectric soft matter in confined space and provide a platform for designing and regulating fluidic polarization macrostructures.

Materials and methods

Materials

RM734, A2, and a side-chain-type chiral dopant S1 were synthesized in the laboratory. The purity of the chemicals was confirmed by NMR and differential scanning calorimetry (DSC) measurements. The commercial chiral dopants S811 and R811 were purchased from TCI (Shanghai) Development Co., Ltd. A room-temperature stable ferroelectric nematic material was prepared by mixing RM734 and A2 at a mass ratio of 1:1 as reported in Long et al. (52). The HN* LCs were obtained by doping chiral dopants into pure RM734, pure A2, or RM734/A2 mixture (Scheme S1). The chiral strength of R811 and S1 in RM734 is 14.2 and 5.5 μm^{-1} , respectively. We notice that a slight doping of R811 into the polar host LCs leads to serious phase separation (i.e. over 3 wt% for R811/A2 mixture), which inhibits the formation of PPW. Therefore, to obtain PPW in shorter-pitch HN* materials (Fig. 2F; Fig. S18), we used S1, which has a similar molecular structure to RM734 and A2 (Scheme S1).

LC cell preparation

The prepared LCs were introduced into homemade LC cells with controlled thickness and surface conditions. A planar anchoring

agent (KPI-3000, Shenzhen Haihao Technology Co., Ltd.) was coated onto the cleaned glass substrates by spin-coating under 3,000 rpm/min. After baking at 200°C for 2 h, a unidirectional rubbing was conducted on each substrate. We assembled two rubbed substrates by aligning their rubbing direction in the same way and obtained a LC cell with the syn-parallel rubbing. The thickness of LC cells was controlled by silica particles in the range of 5–50 μm . The homemade syn-rubbed wedge cell was in the range of 0–150 μm controlled by Teflon films.

Fluorescence confocal polarizing microscopic measurement

FCPM observation was performed using a Zeiss LSM880 microscope. Bis(2,5-di-tert-butylphenyl)-3,4,9,10-perylenedicarboximide (BTBP, Sigma-Aldrich) was used as a fluorescent dye mixed into the LCs. The concentration of BTBP dye was 0.01 wt%. The Ar laser ($\lambda = 488 \text{ nm}$) was used to excite the fluorescence of BTBP, and the fluorescence signal was detected by a photomultiplier tube (PMT) detector in a spectral range of 510–550 nm.

Confocal second harmonic generation microscopic measurement

A femtosecond laser (Coherent Chameleon Vision II; $\lambda = 880 \text{ nm}$; pulse width: 140 fs) was used as the incident laser in the Zeiss LSM880 microscope for the C-SHGM test. The SH signals generated by the HN* samples were collected with a scanning system composed of a 63 \times (NA = 1.4) objective. A gallium arsenide phosphide (GaAsP) and PMT were used for measuring the magnitude of the SH signal.

HL measurement

The spontaneous polarization P_0 was evaluated by measuring the hysteresis loop (HL) curves of the HN* LCs. The HL curves were tested by a triangular wave method (FCE10-F, TOYO Corporation) using 10- μm cells sputtered with indium tin oxide electrodes. The alternative current electric field is supplied along the surface normal of the LC cells at 200 Hz under a peak voltage of 20 Vpp.

Supplementary material

Supplementary material is available at PNAS Nexus online.

Funding

S.A. and M.H. acknowledge the National Key Research and Development Program of China (No. 2022YFA1405000), the Recruitment Program of Guangdong (No. 2016ZT06C322), and the 111 Project (No. B18023). S.A. acknowledges the support from the International Science and Technology Cooperation Program of Guangdong Province (No. 2022A0505050006), the General Program of Guangdong Natural Science Foundation (No. 2022A1515011026), and the Fundamental Research Funds for the Central University (No. 2022ZYGXZR001). M.H. acknowledges the support from the National Natural Science Foundation of China (NSFC No. 52273292).

Author contributions

S.A. designed and directed the research. J.Z. made material characterizations and structural analyses. Y.Z. conducted the theoretical analyses. J.L. and M.H. synthesized the liquid crystal

materials. J.Z., Y.Z., and S.A. wrote the manuscript. All the authors discussed and amended about the manuscript.

Data availability

All study data are included in the article and/or [supplementary material](#).

References

- Khan HR. 2003. Ferromagnetism. In: Meyers RA, editors. *Encyclopedia of physical science and technology*. Third Edition. New York: Academic Press. p. 759–768.
- Said SBM, Sabri MFM, Salleh F. 2021. Ferroelectrics and their applications. Reference Module in Materials Science and Materials Engineering.
- Cheong S-W, Mostovoy M. 2007. Multiferroics: a magnetic twist for ferroelectricity. *Nat Mater*. 6:13–20.
- Parkin SSP, Hayashi M, Thomas L. 2008. Magnetic domain-wall racetrack memory. *Science* 320:190–194.
- Fert A, Cros V, Sampaio J. 2013. Skyrmions on the track. *Nat Nanotechnol*. 8:152–156.
- Thiaville A, Miltat J, Rohart S. 2021. Magnetism and topology. In: Finocchio G, Panagopoulos C, editors. *Magnetic skyrmions and their applications*. Cambridge: Woodhead Publishing. p. 1–30.
- Chang L-J, et al. 2018. Ferromagnetic domain walls as spin wave filters and the interplay between domain walls and spin waves. *Sci Rep*. 8:1.
- Sluka V, et al. 2019. Emission and propagation of 1D and 2D spin waves with nanoscale wavelengths in anisotropic spin textures. *Nat Nanotechnol*. 14:328–333.
- Rezende SM. 2020. Spin waves in ferromagnets: semiclassical approach. In: Rezende SM, editors. *Fundamentals of magnonics*. Cham: Springer International Publishing. p. 31–70.
- Mühlbauer S, et al. 2009. Skyrmion lattice in a chiral magnet. *Science* 323:915–919.
- Kurumaji T, et al. 2019. Skyrmion lattice with a giant topological Hall effect in a frustrated triangular-lattice magnet. *Science* 365: 914–918.
- Tan A, et al. 2016. Topology of spin meron pairs in coupled Ni/Fe/Co/Cu(001) disks. *Phys Rev B*. 94:014433.
- Wintz S, et al. 2013. Topology and origin of effective spin meron pairs in ferromagnetic multilayer elements. *Phys Rev Lett*. 110: 177201.
- Giordano A, et al. 2014. Micromagnetic study of spin-transfer-driven vortex dipole and vortex quadrupole dynamics. *IEEE Trans Magn*. 50:1–4.
- Pribiag VS, et al. 2007. Magnetic vortex oscillator driven by d.c. spin-polarized current. *Nat Phys*. 3:498–503.
- Siracusano G, et al. 2016. Magnetic radial vortex stabilization and efficient manipulation driven by the Dzyaloshinskii–Moriya interaction and spin-transfer torque. *Phys Rev Lett*. 117:087204.
- Das S, et al. 2019. Observation of room-temperature polar skyrmions. *Nature* 568:368–372.
- Khalyavin DD, et al. 2020. Emergent helical texture of electric dipoles. *Science* 369:680–684.
- Han L, et al. 2022. High-density switchable skyrmion-like polar nanodomains integrated on silicon. *Nature* 603:63–67.
- Zhu R, et al. 2022. Dynamics of polar skyrmion bubbles under electric fields. *Phys Rev Lett*. 129:107601.
- Mandle RJ, Cowling SJ, Goodby JW. 2017. A nematic to nematic transformation exhibited by a rod-like liquid crystal. *Phys Chem Chem Phys*. 19:11429–11435.
- Nishikawa H, et al. 2017. A fluid liquid-crystal material with highly polar order. *Adv Mater*. 29:1702354.
- Chen X, et al. 2020. First-principles experimental demonstration of ferroelectricity in a thermotropic nematic liquid crystal: polar domains and striking electro-optics. *Proc Natl Acad Sci U S A*. 117: 14021–14031.
- Li J, et al. 2021. Development of ferroelectric nematic fluids with giant- ϵ dielectricity and nonlinear optical properties. *Sci Adv*. 7: eabf5047.
- Li J, et al. 2021. How far can we push the rigid oligomers/polymers toward ferroelectric nematic liquid crystals? *J Am Chem Soc*. 143: 17857–17861.
- Yang J, et al. 2022. Spontaneous electric-polarization topology in confined ferroelectric nematics. *Nat Commun*. 13:7806.
- Basnet B, et al. 2022. Soliton walls paired by polar surface interactions in a ferroelectric nematic liquid crystal. *Nat Commun*. 13:3932.
- Nazarenko KG, et al. 2023. Chiral ferromagnetic liquid crystals: a physico-chemical analysis of phase transitions and induced helical twisting. *Liq Cryst*. 50:98–109.
- Liu Y, et al. 2018. Ferroelectric polymers exhibiting behaviour reminiscent of a morphotropic phase boundary. *Nature* 562:96–100.
- Guo M, et al. 2021. Toroidal polar topology in strained ferroelectric polymer. *Science* 371:1050–1056.
- Rößler UK, Bogdanov AN, Pflüderer C. 2006. Spontaneous skyrmion ground states in magnetic metals. *Nature* 442:797–801.
- Nagaosa N, Tokura Y. 2013. Topological properties and dynamics of magnetic skyrmions. *Nat Nanotechnol*. 8:899–911.
- Ackerman PJ, Smalyukh II. 2017. Diversity of knot solitons in liquid crystals manifested by linking of preimages in torons and hopfions. *Phys Rev X*. 7:011006.
- Pišljarić J, et al. 2022. Blue phase III: topological fluid of skyrmions. *Phys Rev X*. 12:011003.
- Nych A, Fukuda J-I, Ognysta U, Žumer S, Muševič I. 2017. Spontaneous formation and dynamics of half-skyrmions in a chiral liquid-crystal film. *Nat Phys*. 13:1215–1220.
- Zhao X, et al. 2021. Spontaneous helielectric nematic liquid crystals: electric analog to helimagnets. *Proc Natl Acad Sci U S A*. 118: e2111101118.
- Zhao X, et al. 2022. Nontrivial phase matching in helielectric polarization helices: universal phase matching theory, validation, and electric switching. *Proc Natl Acad Sci U S A*. 119:e2205636119.
- De Gennes P-G, Prost J. 1993. *The physics of liquid crystals*. Marston: Oxford University Press.
- Senyuk BI, Smalyukh II, Lavrentovich OD. 2006. Undulations of lamellar liquid crystals in cells with finite surface anchoring near and well above the threshold. *Phys Rev E*. 74:011712.
- Aharoni H, et al. 2017. The smectic order of wrinkles. *Nat Commun*. 8:15809.
- Sano K, et al. 2021. Propagating wave in a fluid by coherent motion of 2D colloids. *Nat Commun*. 12:6771.
- Blanc C, et al. 2023. Helfrich–Hurault elastic instabilities driven by geometrical frustration. *Rev Mod Phys*. 95:015004.
- Sebastián N, et al. 2020. Ferroelectric–ferroelastic phase transition in a nematic liquid crystal. *Phys Rev Lett*. 124:037801.
- Varney MCM, Zhang Q, Senyuk B, Smalyukh II. 2016. Self-assembly of colloidal particles in deformation landscapes of electrically driven layer undulations in cholesteric liquid crystals. *Phys Rev E*. 94:042709.

- 45 Gong F-H, et al. 2021. Atomic mapping of periodic dipole waves in ferroelectric oxide. *Sci Adv.* 7:eabg5503.
- 46 Faridi E, Kim SK, Vignale G. 2022. Atomic-scale spin-wave polarizer based on a sharp antiferromagnetic domain wall. *Phys Rev B.* 106:094411.
- 47 Prabhakar A, Stancil DD. 2009. *Spin waves: theory and applications.* New York: Springer.
- 48 Smalyukh II, Lavrentovich OD. 2002. Three-dimensional director structures of defects in Grandjean–Cano wedges of cholesteric liquid crystals studied by fluorescence confocal polarizing microscopy. *Phys Rev E Stat Nonlin Soft Matter Phys.* 66:051703.
- 49 Pieranski P. 2021. Cholesteric dislocations in mica wedges. *Liquid Crystals Reviews.* 1–28.
- 50 Yu M, Yang H, Yang DK. 2017. Stabilized electrically induced Helfrich deformation and enhanced color tuning in cholesteric liquid crystals. *Soft Matter.* 13:8728–8735.
- 51 Deng L, et al. 2020. Room-temperature skyrmion phase in bulk Cu_2OSeO_3 under high pressures. *Proc Natl Acad Sci U S A.* 117: 8783–8787.
- 52 Long H, Li J, Huang M, Aya S. 2022. Mixing-induced phase stabilization and low-temperature-shifting of ferroelectric nematics. *Liq Cryst.* 49:2121–2127.